Materials Characterization 178 (2021) 111240

Contents lists available at ScienceDirect

Materials Characterization

journal homepage: www.elsevier.com/locate/matchar

Synergistic effects of γ-Al_2O_3 nanoparticles and fast cooling on the microstructural evolution and mechanical properties of Al-20Si alloys

Gaopeng Xu, Kui Wang *, Xun Lv, Haonan Li, Haiyan Jiang *, Qudong Wang, Wenjiang Ding

National Engineering Research Center of Light Alloy Net Forming, State Key Laboratory of Metal Matrix Composites, Shanghai Jiao Tong University, 200240 Shanghai, PR China

ARTICLE INFO

Keywords:
Hypereutectic Al-20Si alloy
Nanoparticle distribution
Cooling rates
Refinement and modification
Mechanical properties

ABSTRACT

Hypereutectic Al-Si alloys have been applied as structural materials in various fields thanks to their favorable wear resistance, good thermal conductivity and low coefficient of thermal expansion. Nevertheless, such alloys usually have poor strength and ductility because the coarse primary Si and acicular eutectic Si in the matrix can severely degrade the mechanical properties. Thus, the control over the alloy microstructure is crucial in achieving the enhanced mechanical performance. Herein, we demonstrate that the size, distribution and morphology of primary and eutectic Si phases can be changed upon the addition of γ-Al_2O_3 nanoparticles (NPs) and further tailored by tuning cooing rates. The addition of NPs combined with the fast-cooling treatment can induce the phenomenal refinement and modification of Si phases in Al-20Si alloys. The NP-induced refinement and modification mechanisms have been proposed to elucidate the microstructural evolution of Al-20Si alloys produced at various cooling rates. Results indicate that the Al-20Si alloys with the addition of 2.0 wt% NP produced at the cooling rate of 100 K/s can exhibit the most excellent mechanical properties with their yield strength, ultimate tensile strength, elongation and microhardness improved by 78.0%, 75.5%, 301.7% and 119.3%, respectively, in comparison with Al-20Si alloys produced via the conventional casting route.

1. Introduction

Hypereutectic Al-Si alloys have been extensively used as structural materials in automotive, military and electronic industries thanks to their favorable wear resistance, good thermal conductivity and low coefficient of thermal expansion [1–3]. In the case of the conventional casting route, the typical morphology of hypereutectic Al-Si alloys is composed of coarse irregular-shaped primary Si and flake-like eutectic Si [4,5]. The inhomogeneous and coarse microstructure tends to induce stress concentration, facilitating the initiation and propagation of crack, which greatly degrades the mechanical properties [6,7]. Consequently, the control over the microstructure of hypereutectic Al-Si alloys is of great importance for their enhanced mechanical performance.

A multitude of methods have been taken to obtain the refined and dispersed Si phases, including chemical modification [8,9], rapid solidification [10–12], mechanical vibration [11,13,14]. Among them, chemical modification is one of the most widely used approach owing to its simplicity and cost-effectiveness. It is well documented that P and Sr are the effective modifiers for the refinement and modification of Si particles, respectively [15–18]. Specifically, P can react with Al to form AlP that can work as a potent nucleating particle for primary Si while Sr can induce the morphological variation of eutectic Si from long acicular to fiber-like structure [17,18]. However, the combination of Sr and P is difficult to accomplish the primary Si refinement and eutectic Si modification simultaneously. Studies showed that Sr can react with P to form Sr_3P_2 [19], decreasing the amount of P and Sr in the melt and thus vitiating the refinement and modification effects of primary Si and eutectic Si, respectively. Even though much research has demonstrated that rare earth elements like Ce [20], Er [21], Sc [22] and Yd [23] can simultaneously refine and modify Si particles, their scarce reserves and active chemistry may impede their wide industrial application.

Apart from the chemical elements, ceramic particles are found to be helpful in improving the microstructure of Si phases in hypereutectic Al-Si alloys. Li et al. [24], introduced the in-situ formed γ-Al_2O_3 particles to hypereutectic Al-20Si alloys through in situ salt-melt reaction method and found that γ-Al_2O_3 particles can refine primary Si from coarse irregular to fine block-like structure and eutectic Si from long acicular to refined flake-like structure through heterogeneous nucleation and suppression growth mechanisms. Choi et al. [25] demonstrated that γ-Al_2O_3 NPs incorporated ultrasonically into Al-Si melts can simultaneously

* Corresponding authors.
E-mail addresses: fateratory@sjtu.edu.cn (K. Wang), jianghy@sjtu.edu.cn (H. Jiang).

https://doi.org/10.1016/j.matchar.2021.111240
Received 18 January 2021; Received in revised form 2 May 2021; Accepted 30 May 2021
Available online 4 June 2021

induce the refinement of primary Si and the modification of eutectic Si in Al-20Si alloys, respectively. However, compared with the marked refinement of primary Si, the modification of eutectic Si appears not so prominent in their work, with many acicular eutectic Si prevailing in the matrix. Currently, the main refinement and modification mechanisms induced by NPs can be concluded as (i) NPs can function as the heterogeneous nucleating particles for Si particles to promote their nucleation [5,25,26]; (ii) NP assembly on the surface of Si particles can restrict their growth [27]; (iii) NPs induce the poison of the twin plane re-entrant edge (TPRE), causing a growth transformation of eutectic Si from the anisotropy to isotropy [6]. In fact, as one of the dominating factors determining the refinement and modification effects, the NP distribution may vary with the cooling rate of the alloy. Although the proposed mechanisms can account for the refinement or modification phenomenon in a certain case, few efforts have been made to investigate the NP effects on size, distribution and morphology of Si phases at a wide range of cooling rates. More importantly, studies [11,16,28] revealed that an increased cooling rate of Al-Si alloys may provide sufficient undercooling for the heterogeneous nucleation of Si phases in the melt to promote their refinement. As a result, the addition of NP combined with the fast-cooling treatment may provide a promising avenue for the further improvement in the microstructure and performance of hypereutectic Al-Si alloys. Hence, it is indispensable to investigate the influences of the added NPs and cooling rates on the growth behavior of Si particles and to unveil the NP-induced growth mechanisms of Si phases, especially at fast cooling rates.

Due to the presence of the oxide layer on liquid aluminum, the poor wetting of γ-Al_2O_3 NPs by liquid aluminum occurs at the casting temperatures. Thereby, it is difficult to add γ-Al_2O_3 NPs directly to the Al melt [27]. Studies [11,27,29] indicated that ultrasonic treatment is effective in disrupting Al oxide films, improving the wettability of NPs and thus dispersing them in the melts. In this work, hypereutectic Al-20Si alloys containing different contents of γ-Al_2O_3 NPs have been synthesized via ultrasonic melt treatment combined with fast cooling technique. Extensive characterization has been performed to reveal the microstructural evolution of Si phases as well as the distribution of NPs. On the basis of the experimental results, the NP-induced refinement and modification mechanisms have been proposed to elucidate the microstructural evolution of hypereutectic Al-20Si alloys solidified at different cooling rates. Furthermore, the influences of NPs and cooling rates on the mechanical performance of the Al-20Si alloys were also analyzed.

2. Experimental

2.1. Material preparation

Hypereutectic Al-20Si (wt%) alloys were synthesized with an electronic resistance furnace. Pure aluminum and silicon were used as the raw materials. For purpose of removing gases and oxides, Al-20Si melts were degassed with 0.5 wt% C_2Cl_6 for 3–5 min at 993–1013 K. After skimming off the oxide skin, γ-Al_2O_3 NPs (commercially available) wrapped in aluminum foils were slowly added into the melts. Fig. 1b gives a statistical diagram of the size distribution of γ-Al_2O_3 NPs, and the size distribution mainly ranges from 20 to 40 nm. The ultrasonic vibration treatment was introduced into the melt to disperse the NPs as shown in Fig. 1a. Once the temperature of the melt was drop to 933 K, the ultrasonic horn made from ceramic matrix composites preheated to 423 K was inserted in depth of 10–15 mm into the melt. The whole ultrasonic processing lasted for 15 min with the protection of argon gas. After dispersing γ-Al_2O_3 NPs, the ultrasonic horn was taken out. Actually, the same ultrasonic melt treatment was also performed on the Al-20Si alloy without γ-Al_2O_3 NP addition to avoid the effect of ultrasonic treatment on the refinement of Si. Then the melt was reheated to 1013 K and poured into a cast iron mold with the dimension of 200 × 150 × 20 mm^3 preheated to 623 K. The determined cooling rate was around 5 K/s with a thermocouple inserted into the mold, and the specific cooling curves are displayed in Fig. S1. To in-depth analyze the influences of γ-Al_2O_3 NPs on the microstructural evolution of hypereutectic Al-20Si alloys at different cooling rates, the copper mold and the copper mold equipped with circulating water-cooling device were used to provide fast cooling rates for casting alloys, and the cooling rates were determined to be about 50 and 100 K/s, respectively.

2.2. Microstructural characterization

After being sanded with sandpaper and polished, specimens were etched with Keller's reagent, then examined by optical microscope (OM; Nikon, MA200). The average size and the corresponding aspect ratio of primary Si particles as well as those of eutectic Si were measured using Image-Pro Plus 6.0. The three-dimensional (3D) microstructure, especially the distribution of Si particles in Al-20Si + 2NP alloys (Al-20Si alloy containing 2.0 wt% NP) were investigated using the X-ray microscope (Zeiss Xradia 520 Versa). Then the analysis and processing of 3D information were conducted using 3D analysis software (Zeiss Dragonfly), which contains image fragmenting and 3D mesh reconstruction of Si particles. The microstructure and the distribution of NPs were

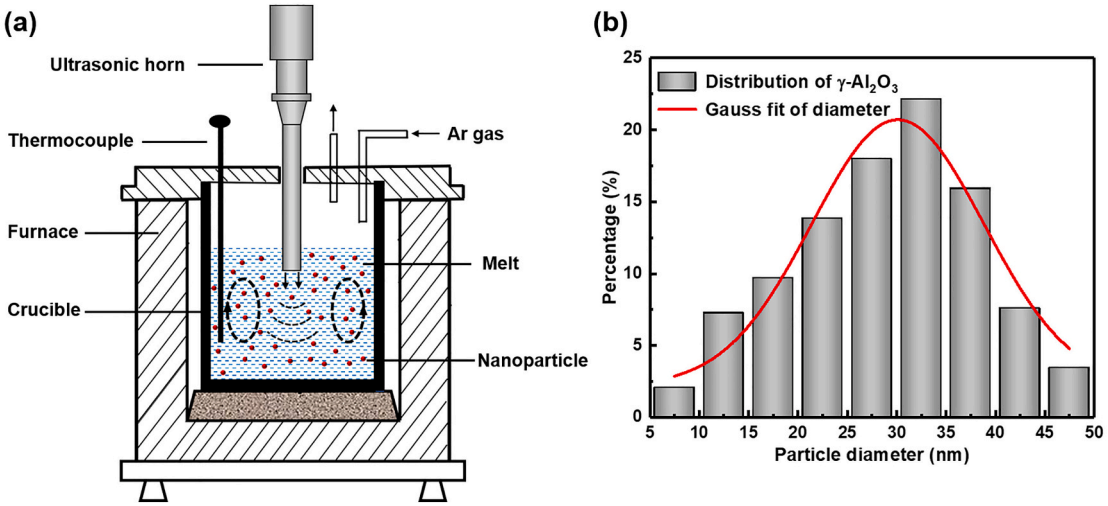

Fig. 1. (a) Schematic illustration of the experimental setup; (b) Size distribution of γ-Al_2O_3 NPs.

characterized with the scanning electron microscope (SEM; TESCAN MIRA 3, Czech) equipped with an energy dispersive X-ray spectroscopy (EDS; AZtec X-MaxN80) module. Transmission electron microscopy (TEM, JEOL-2100 F) was used to examine the NP distribution, chemical compositions, crystal structures and orientation relationships of the γ-Al_2O_3 NPs with the Si particle. TEM foils were fabricated by the Gatan model 695 precision ion polishing system.

2.3. Mechanical properties

Hardness and elastic modulus of the Si particles were evaluated with Agilent Nano Indenter G200 at a fixed load rate of 10 μN/s up to a pre-set peak value 1500 μN with the Berkovich diamond indenter. Each test result is an average of five readings. Tensile tests were operated on a tensile testing machine (Zwick/Roell Z100). Each result was taken from an average of 3 readings. The microhardness of the sample was conducted by a HDX-1000 Vickers hardness tester with a load of 0.98 N for a dwell time of 20 s. Each reported hardness value is determined as the average value of five measurements.

3. Results and discussion

3.1. Microstructural evolution of primary and eutectic Si

The as-cast microstructure of Al-20Si alloys with different NP additions was given in Fig. 2. As shown in Fig. 2a, it is evident that the NP-free Al-20Si alloy has a coarse and inhomogeneous microstructure. The primary Si exists with irregular shapes including polygonal, star-like and complex ones while the eutectic Si with a long acicular structure as displayed in the inset of Fig. 2a. According to the histograms in Fig. 2e and f, the average size and aspect ratio of unrefined primary Si are 66.2 μm and 2.5, respectively, and the average length of unmodified eutectic Si is 67.5 μm. After 2.0 wt% NP addition, the primary Si is significantly refined, whose average size and aspect ratio are reduced to 26.8 μm and 1.6, respectively, as shown in Fig. 2e. A remarkable morphological transformation of primary Si particle from the coarse block-like to fine spherical phase is clearly given in Fig. 2a–d. Additionally, the influence of NPs on the length and the micromorphology of the eutectic Si is also presented in the insets in Fig. 2a–d and Fig. 2f. Despite a marked reduction of the eutectic Si length from 67.5 to 26.1 μm, its morphology varies slightly and the majority are still in the shape of elongated structure with sharp edges, which is detrimental to the mechanical performance. In general, γ-Al_2O_3 NPs can make a great contribution to the primary Si refinement and concomitantly cause an insufficient eutectic Si modification in Al-20Si alloys.

Fig. 3 is the microstructure of the Al-20Si alloys and Al-20Si + 2NP alloys prepared at different cooling conditions. It is found that the average sizes of the primary Si in both alloys decrease with the cooling rate increasing. When the cooling rate increasing from 5 to 100 K/s, the average size and aspect ratio of primary Si in Al-20Si + 2NP alloys are decreased from 26.8 μm and 1.6 to 15.8 μm and 1.28, respectively. By comparison, the cooling rate may have a more remarkable effect on the refinement of primary Si in the matrix alloy, whose average size and aspect ratio are reduced from 66.2 μm and 2.5 to 25.4 μm and 1.6, respectively. However, unlike the primary Si in the matrix alloy, which still shows star-like or block-like morphology even at high cooling rates, the fine spherical primary Si particles prevail in the matrix of Al-20Si + 2NP alloy produced at different cooling conditions as shown in Fig. 3d–f. It can be implied that the enhanced refining effect of primary Si in Al-20Si + 2NP alloy may be attributed to synergistic effects from the NP addition and fast cooling processing. The insets in Fig. 3a–f illustrate the evolution of the size and morphology of eutectic Si in both alloys solidified at various cooling rates. With the increase of cooling rate from 5 to 100 K/s, the eutectic Si particles in Al-20Si alloy are further refined while maintaining the elongated structure. Statistically, their average size is reduced from 68.2 to 24.8 μm. In contrast, eutectic Si particles achieve a sufficient modification in Al-20Si + 2NP alloy solidified at the cooling rate of 100 K/s. The morphology of eutectic Si transforms obviously from long acicular to fine fiber-like structure, as observed in Fig. 3d–f. In Fig. 3h, the average length of eutectic Si declines from 26.8 to 4.6 μm with the cooling rate increasing from 5 to 100 K/s. The result reveals that the addition of γ-Al_2O_3 NPs accompanied with the fast cooling processing can induce a significant refinement of primary Si and a sufficient modification of eutectic Si, which is different from the findings of Choi et al [25].

Given the information provided by 2D micrographs may not be used to evaluate the 3D spatial distribution of Si particles, 3D tomography analysis is performed to visualize the spatial distribution of Si particles in the sample. Fig. 4 gives two observation areas with the same dimensions selected from Al-20Si + 2NP alloys prepared at the cooling

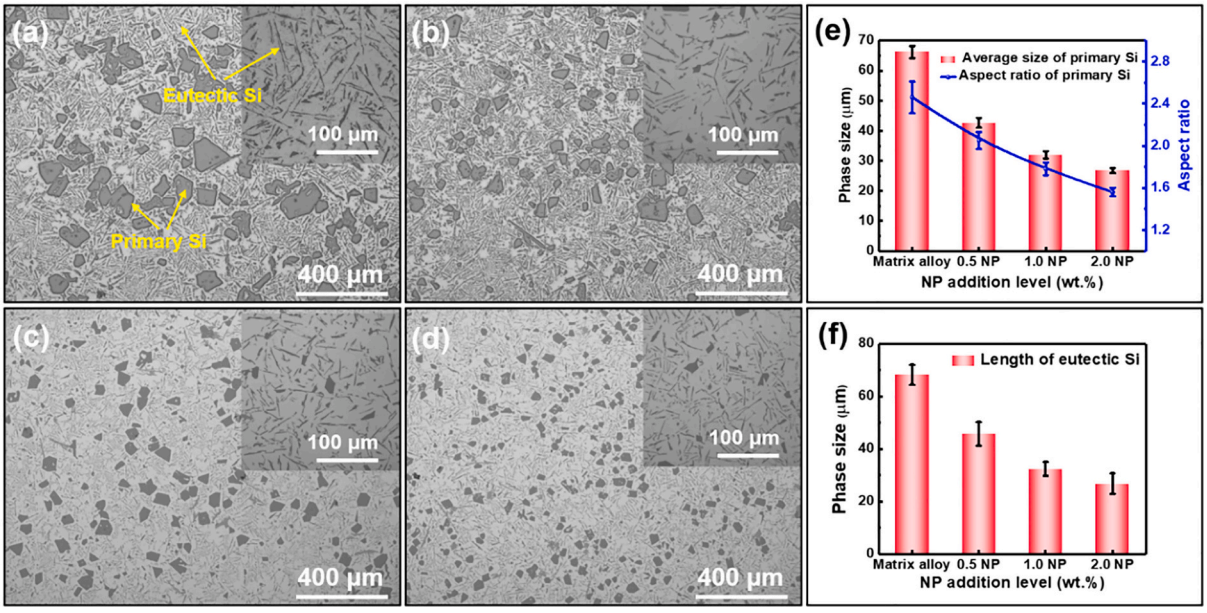

Fig. 2. The microstructures of Al-20Si alloys with various γ-Al_2O_3 NPs addition levels. (a) Matrix alloy; (b) 0.5 wt%; (c) 1.0 wt%; (d) 2.0 wt%. (e) Size and aspect ratio distribution of primary Si with different NP addition levels; (f) Size distribution of eutectic Si with different NP addition levels.

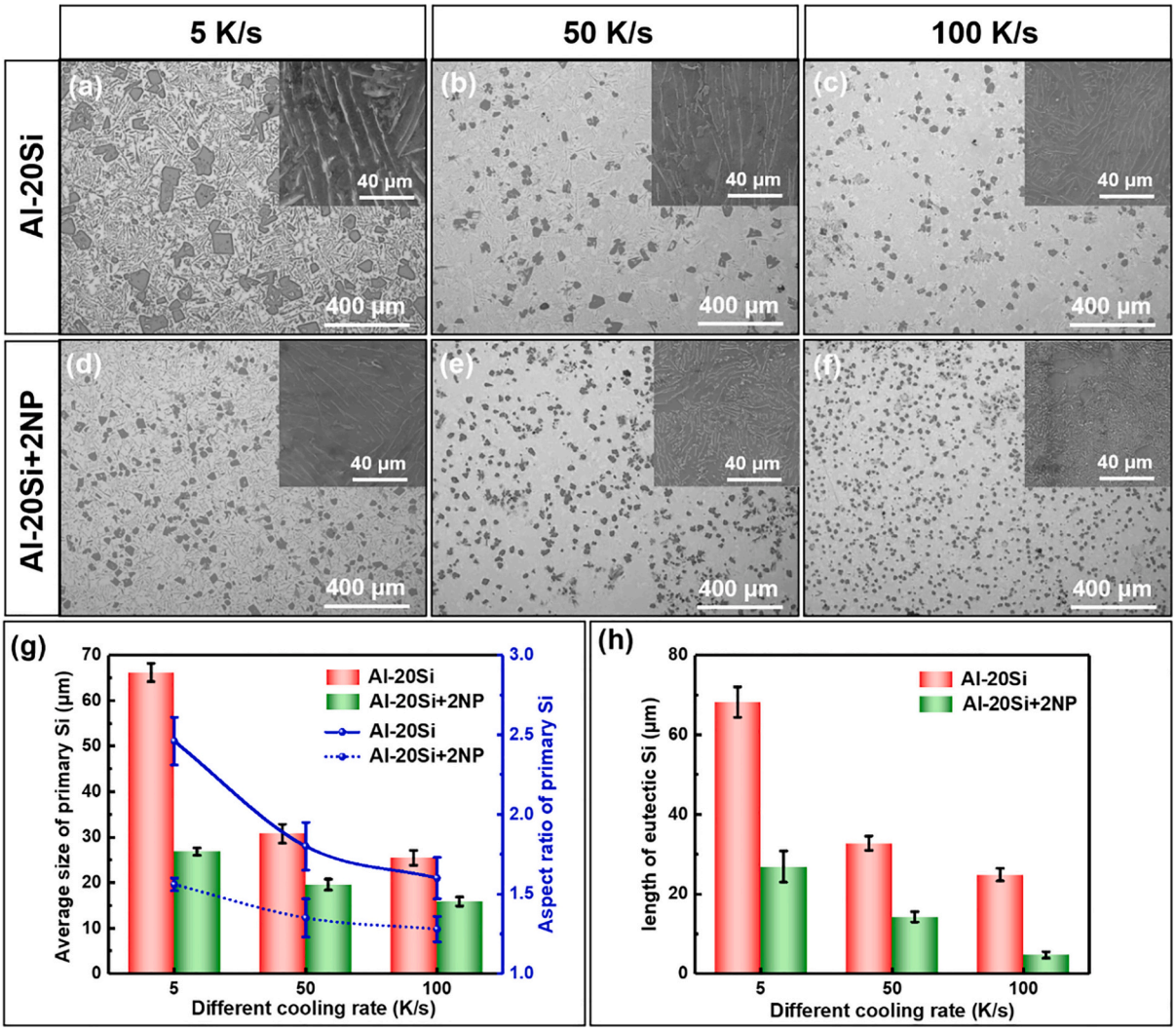

Fig. 3. The solidification microstructures of Al-20Si alloys with and without 2.0 wt% NP addition at different cooling rates. (a)–(c) Solidification microstructures of Al-20Si alloys solidified at the cooling rates of 5 K/s, 50 K/s and 100 K/s, respectively. (d)-(f) Solidification microstructures of Al-20Si + 2NP alloys solidified at the cooling rates of 5 K/s, 50 K/s and 100 K/s, respectively. (g) Size and aspect ratio distribution of primary Si particles; (h) Size distribution of eutectic Si.

rate of 5 and 100 K/s, respectively. As indicated in Fig. 4a and f, α-Al matrix is colored in blue, while Si particles dispersed in the matrix are distinguished in green. Fig. 4b–e and Fig. 4g–j are the partial morphology and the corresponding Si particle distribution extracted from Fig. 4a and Fig. 4f, respectively. Among them, the partial 3D microstructure and the corresponding Si particle morphology can be obtained from the 2D images via reconstruction, extraction and visualization. Fig. 4e and j represent the spatial morphology and distribution of Si particles extracted from Fig. 4d and i, respectively. As clear from Fig. 4e and j, it is manifested that the average size of Si particles in Al-20Si + 2NP alloy produced at 100 K/s is obviously smaller than that at 5 K/s. Additionally, the morphology of Si particles is more regular, and the spatial distribution is more dispersive and homogeneous. Fig. 5a and b are the 3D morphologies of Si particles extracted from two observation areas with the same dimensions randomly selected from Al-20Si + 2NP alloys prepared at the cooling rate of 5 and 100 K/s, respectively. The quantitative statistics result of two 3D images in Fig. 5c displays that the volume fraction of Si particles is increased slightly from 14.8% to 15.9% with the cooling rate increasing from 5 to 100 K/s. Additionally, the specific surface area of Si particles is 0.436 μm^{-1} for the Al-20Si + 2NP alloy produced at 5 K/s, which is much smaller than 0.678 μm^{-1} for that at 100 K/s. The obtained results in 3D micrographs demonstrate that the high cooling rate can further refine Si particles in Al-20Si + 2NP alloys and improve their spatial morphology and distribution simultaneously.

3.2. Evolution of NP distribution

For in-depth understanding the influences of NPs on the microstructural evolution of Si phases, high magnification SEM observation and TEM analysis were conducted to reveal the NP distribution at low and high cooling rates (5 and 100 K/s, respectively).

Fig. 6 presents the NP distribution at the low cooling rate. As displayed in Fig. 6a, a host of NPs assemble onto the phase interface of a primary Si particle, while a few NPs can be detected in the interior of primary Si. Further observation in Fig. 6b shows that the interphase NPs that are distributed along the phase boundary of primary Si agglomerate together to constitute a NP-layer covering the surface of the primary Si particle. The formed NP-layer can be deemed as an effective inhibitor for solute transport onto the growing interface, resulting in a phenomenal refinement of primary Si [29–32]. Some of them marked by a red dotted-box are selected for EDS analysis. According to the result in Fig. 6c, these NP can be basically identified as γ-A_2O_3. Similarly, a large quantity of NPs can be also found to be distributed along the interface boundary of eutectic Si, forming a uniform and dense NP-layer as indicated in Fig. 6d. The High-resolution transmission electron microscope (HRTEM) observation in Fig. 6e indicates that some of them may not contact closely

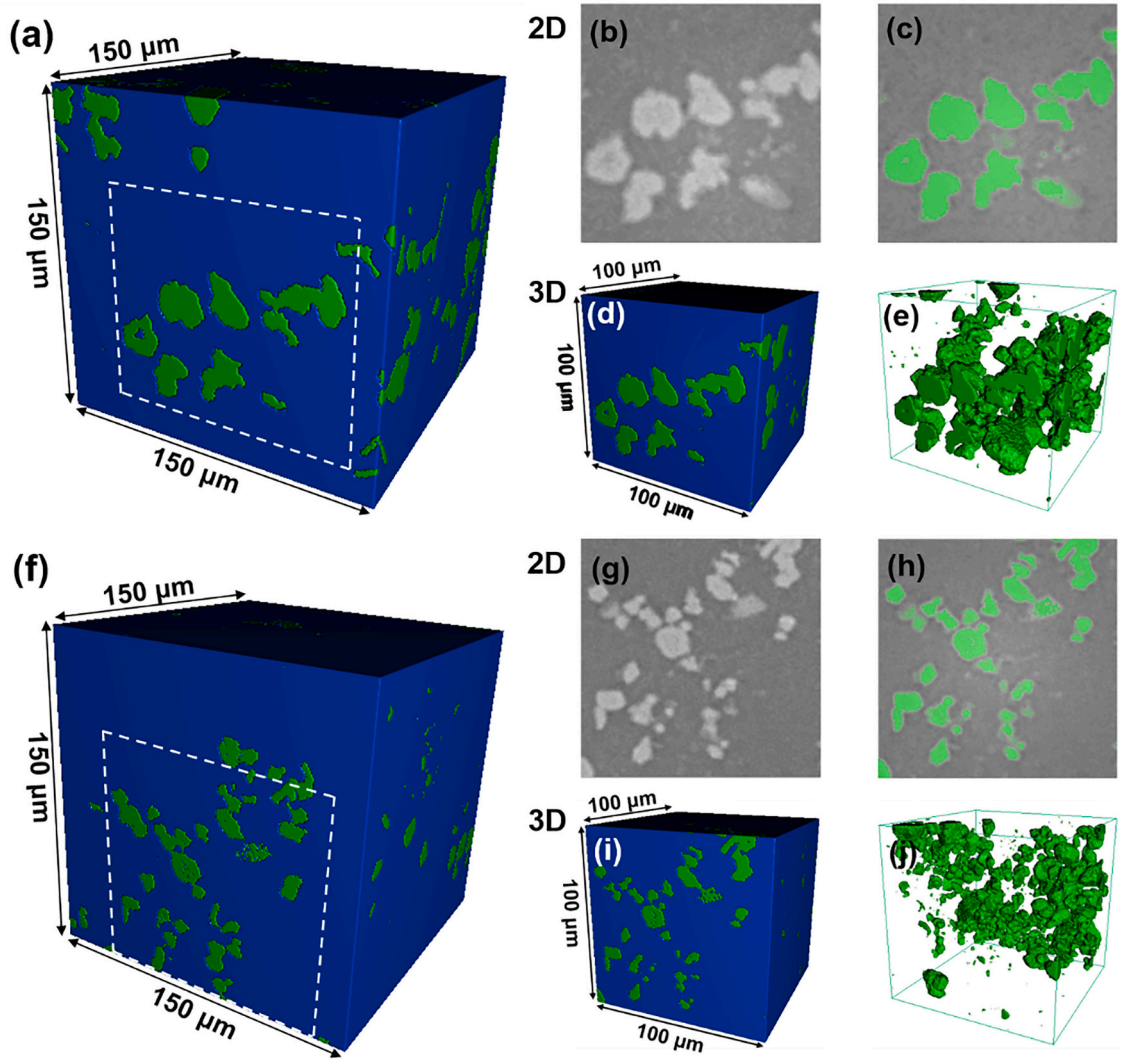

Fig. 4. 3D morphology of the Al-20Si + 2NP alloy solidified at the cooling rate of (a) 5 K/s; (f) 100 K/s; (b) and (c) 2D images extracted from (a); (d) and (e) 3D images extracted from (a); (g) and (h) 2D images extracted from (f); (i) and (j) 3D images extracted from (f).

with one another and a nanochannel between the adjacent NPs is formed, which can effectively restrict the diffusion path of the solute atoms and thereby effectively restrict the growth of eutectic Si [29,30,33]. Furthermore, combined with the HRTEM analysis and the corresponding fast Fourier transformation (FFT) in Fig. 6f, these interphase NPs can be further confirmed as γ-Al_2O_3 and no crystal orientation relationship between γ-Al_2O_3 NPs and eutectic Si particle can be observed. It can be inferred that the interphase NPs are capable of refining Si particles mainly by physically assembling onto their phase surface. However, a coherent interface between the NP and the matrix can be observed in Fig. 6e, and the orientation relationship can be obtained as $(222)_{\gamma\text{-}Al2O3}//(111)_{\alpha\text{-}Al}$, $[1\bar{2}1]_{\gamma\text{-}Al2O3}//[1\bar{2}1]_{\alpha\text{-}Al}$ and $(40\bar{4})_{\gamma\text{-}Al2O3}//(20\bar{2})_{\alpha\text{-}Al}$, $[1\bar{2}1]_{\gamma\text{-}Al2O3}//[1\bar{2}1]_{\alpha\text{-}Al}$. The interfacial coherency demonstrates that there exists a good wettability between the γ-Al_2O_3 NP and the matrix via ultrasonic treatment. It may provide a strong interface adhesion between them, thus enhancing the efficacy of load transfer [30].

Fig. 7 shows the NP distribution at the high cooling rate. With the synergistic effects from NP addition and rapid solidification, the primary Si particle is greatly refined as observed in Fig. 7a. Further observation and EDS mapping were performed on the white dotted-box area. It can be seen that the NP cluster is located in the center of a primary Si particle. As depicted in Fig. 7b, Si, O and Al elements can be detected and thus they are primarily composed of γ-Al_2O_3 NPs. Fig. 7c provides a magnified view of the phase boundary shown in the red dotted-box in Fig. 7a. It is found that different from the interphase distribution of NPs at the low cooling rate, they are distributed in the α-Al matrix but in the vicinity of the phase boundary of the primary Si at the high cooling rate. As can be observed from Fig. 7d, multiple Si twins growing along the ⟨112⟩ growth direction are formed within the eutectic Si. Meanwhile, dozens of NPs distributed within the eutectic Si can be also observed. Fig. 7e is the HRTEM micrograph of a NP in the eutectic Si matrix. It is obvious that the NP is completely coherent with the eutectic Si matrix. Combined with the crystallographic information given by the FFT analysis in Fig. 7f, two specific orientation relationships between the NP and Si can be obtained as $(222)_{\gamma\text{-}Al2O3}//(112)_{Si}$, $[01\bar{1}]_{\gamma\text{-}Al2O3}//[1\bar{1}0]_{Si}$ and $(2\bar{2}2)_{\gamma\text{-}Al2O3}//(11\bar{2})_{Si}$, $[01\bar{1}]_{\gamma\text{-}Al2O3}//[1\bar{1}0]_{Si}$. Accordingly, it can be speculated that γ-A_2O_3 may serve as the potential nucleation sites for Si particles at high cooling rates. Fig. 7g is the TEM micrograph of another eutectic Si particle, where high-density parallel Si micro-twins along the <112> growth direction of Si and a myriad of NPs with the sizes of less than 20 nm can be clearly observed in Fig. 7h. It is displayed that some NPs are entrapped at TPRE. To further reveal the influence of NPs on the TPRE growth of eutectic Si, HRTEM analysis of a single NP entrapped at TPRE is performed in Fig. 7i. Combined with the FFT analysis, it is indicated that the NP entrapped at TPRE is γ-Al_2O_3 and also perfectly

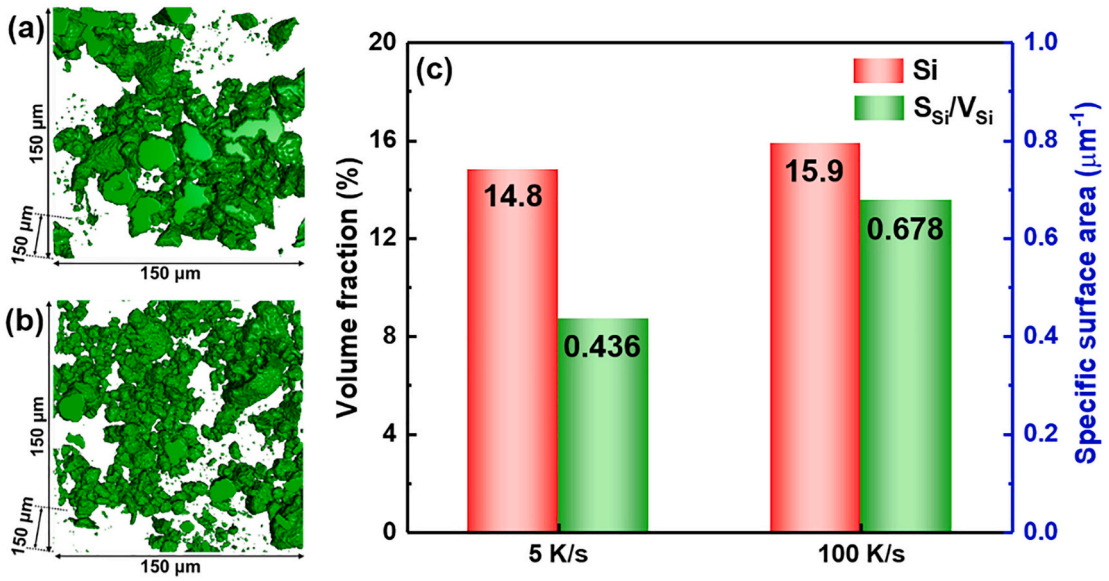

Fig. 5. 3D morphologies of the separated Si particles in the dimension of 150 × 150 × 150 μm^3: (a) 5 K/s; (b) 100 K/s; (c) Volume fraction and specific surface area of Si particles in Al-20Si + 2NP alloys.

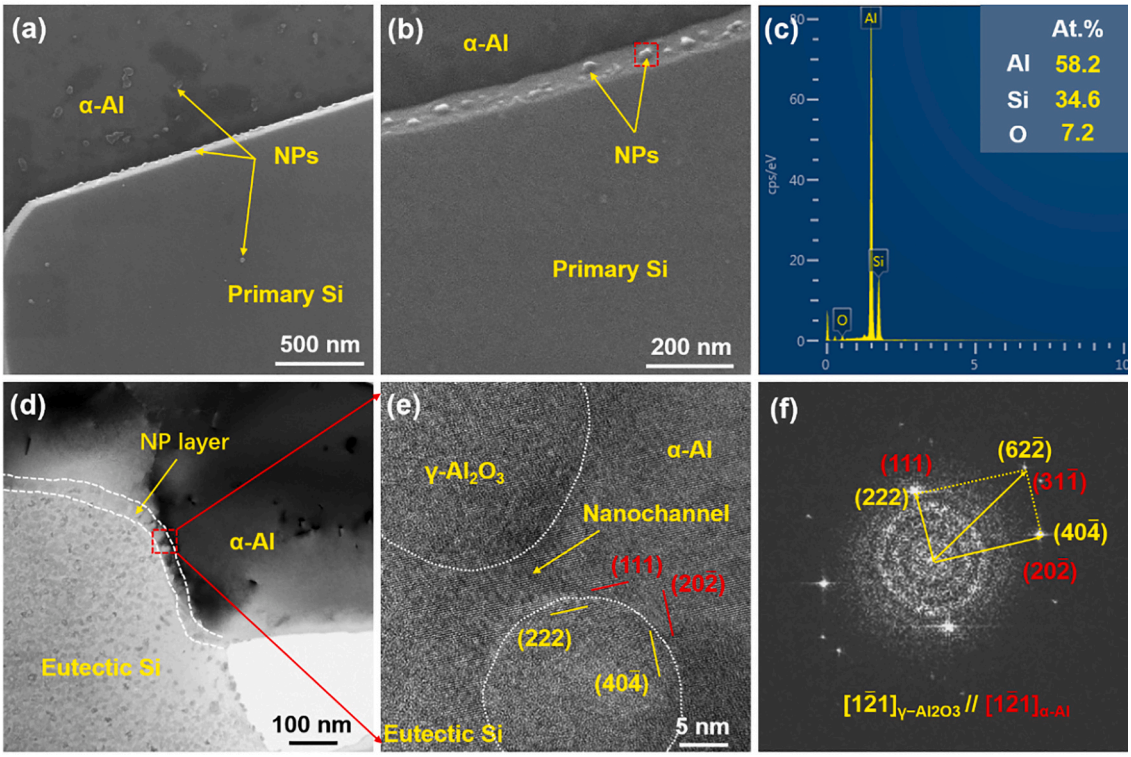

Fig. 6. The microstructure of the Al-20Si + 2NP alloy solidified at the low cooling rate of 5 K/s: (a) SEM micrograph of the primary Si particle and NPs; (b) Magnified view of NPs distributing along the interface between the primary Si and α-Al matrix; (c) EDS spectra of a NP, (d) TEM micrograph showing the NPs dispersed along the eutectic Si; (e) HRTEM images highlighting the NPs distributing at the interface between the eutectic Si and α-Al matrix; (f) FFT analysis of the interface in Fig. 6e.

coherent with the eutectic Si matrix. The specific orientation relationship can be obtained as: $(033)_{γ\text{-}Al2O3}//(220)_{Si}$, $[100]_{γ\text{-}Al2O3}//[1\bar{1}\bar{1}]_{Si}$ and $(01\bar{4})_{γ\text{-}Al2O3}//(0\bar{2}2)_{Si}$, $[100]_{γ\text{-}Al2O3}//[1\bar{1}\bar{1}]_{Si}$.

The nanoindentation test results of Si particles in Al-20Si + 2NP alloys at low and high cooling rates are presented in Fig. 8. It is revealed that the average hardness of primary and eutectic Si are enhanced from 11.8 and 9.1 GPa to 12.3 and 9.9 GPa as the cooling rate increases from 5 K/s to 100 K/s, respectively. Additionally, the elasticity modulus of the primary and eutectic Si particles at different cooling rates are illustrated in Fig. 8b. Modulus variation shows the same response to the cooling rates as the nanoindentation hardness, and the modulus values of primary and eutectic Si particles increase from 176.5 and 118.6 GPa to 182.5 and 139.2 GPa with the enhancement of cooling rate from 5 K/s to 100 K/s, respectively. The inset in Fig. 8a displays the load-displacement curves corresponding to the primary and eutectic Si particles at different

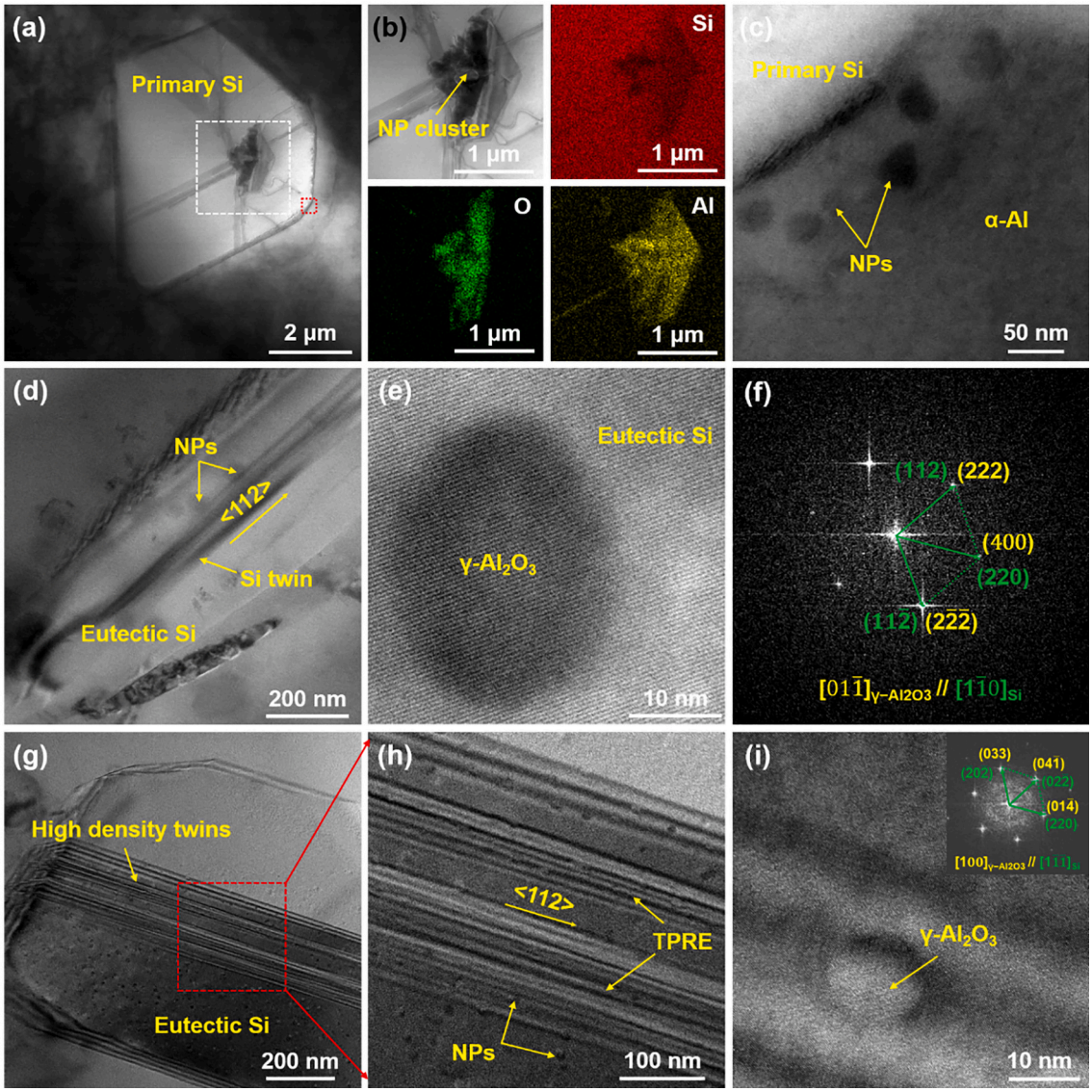

Fig. 7. The microstructure of the Al-20Si + 2NP alloy solidified at the high cooling rate of 100 K/s: (a) TEM bright-field image of a primary Si particle; (b) Magnified image of the white dotted-box in Fig. 7a and the corresponding STEM-EDS mapping analysis; (c) TEM image showing the NPs located in the vicinity of primary Si/α-Al interface; (d) TEM image of a eutectic Si particle; (e) HRTEM image showing the NP in the eutectic Si matrix; (f) FFT analysis of Fig. 7e; (g) TEM bright-field image of another eutectic Si particle; (h) Magnification view showing the NPs located in the eutectic Si; (i) HRTEM analysis of a single NP embedded at the TPRE. The inset is the FFT analysis of Fig. 7i.

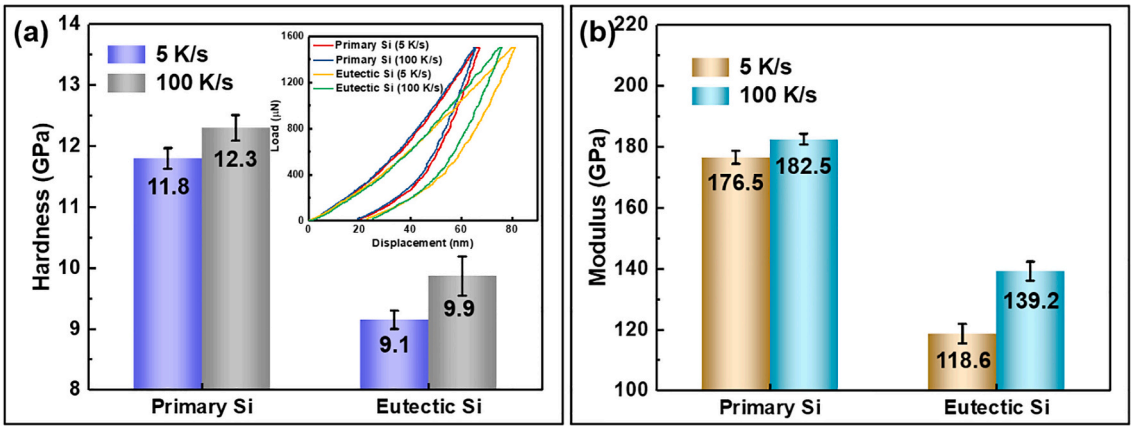

Fig. 8. Nanoindentation test results of Si particles: (a) Hardness; (b) Elasticity modulus; The inset in Fig. 8a showing the load-displacement curves.

cooling rates. It is evident that the indenter penetration depth corresponding to Si particles at the low cooling rate (5 K/s) is slightly larger than that at the high cooling rate (100 K/s), which implies that the Si particles at high cooling rates possess a higher resistance to indentation. On the basis of the microstructure characterization, γ-Al_2O_3 NPs at 5 K/s are distributed along the interface between the Si particle and Al matrix, while those at 100 K/s are dispersed within the Si particles. Consequently, the hard γ-Al_2O_3 NPs inside the Si particle can serve as the effective barriers to impede the dislocation motion across the Si matrix and provide a stronger resistance against the local plastic deformation compared with the Si particle without NPs in the interior, thus imparting enhanced hardness and modulus.

3.3. NP-induced refinement mechanism of primary Si

According to the obtained results and the previous studies [5,24,25], the refinement mechanism of primary Si can be explicated from the perspective of the growth restriction and heterogeneous nucleation. A number of studies [6,24,25] suggested that there exists a small lattice disregistry of 3% between γ-Al_2O_3 particle and Si phase, implying that the γ-Al_2O_3 NPs may become the potential nucleation sites for primary Si particles to promote their heterogeneous nucleation. Nevertheless, apart from a desirable crystallographic matching, the sufficient undercooling of melt is an alternative important factor in determining the nucleation potency of particles [34]. In terms of athermal heterogeneous nucleation theory, the critical nucleation undercooling degree (ΔT) depending on the size of nucleant particles (d) can be given by $\Delta T \approx \frac{4\gamma_{SL}T_m}{L_v d}$ [35], where γ_{SL} is the interfacial energy between Si particle and melt, L_v is the latent heat of fusion, and T_m is the melting point. In this work, $\gamma_{SL} = 0.41$ J/m^2 [36], L_v is taken to be 6.28×10^8 J/m^3 [37], $T_m = 947$ K [11]. As indicated in Fig. 1b, given that the size distribution of γ-Al_2O_3 NPs incorporated into the melt is almost less than 50 nm, the undercooling required for heterogeneous nucleation of primary Si is determined to be at least 49.46 K. However, the actual undercooling under routine solidification conditions is far less than the required critical undercooling [6], and thus the individual γ-Al_2O_3 NPs may not serve as the valid nucleation sites for primary Si at low cooling rates, despite the high nucleation potency. Nevertheless, apart from the individual NPs dispersed in the melt, some of the NPs will inevitably agglomerate to form NP clusters even under ultrasonic treatment. The larger size of NP clusters greatly reduces the critical undercooling. Therefore, the heterogeneous nucleation of primary Si induced by NP clusters would occur even at low cooling rates.

On the other hand, whether γ-Al_2O_3 NPs would be pushed or engulfed by the solidification front is mainly dominated by the interaction between NPs and the ongoing solidification fronts during solidification [38]. A critical velocity is often used to decide the pushing/engulfment behavior of NPs by a growing solid/liquid interface: when the growing interface velocity less than the critical velocity, NPs would be pushed by the growing interface; when the interface velocity larger than the critical velocity, NPs would be engulfed by the growing interface [27,39]. Previous research [29,39,40] demonstrates that under routine solidification conditions, the solidification rates of melts are often quite low, thus leading to the growing interface velocity far less than the required critical velocity. Thereby, γ-Al_2O_3 NPs are highly possible to be pushed by the growing interface at low solidification rates, whereas they may be engulfed at high solidification rates, which is in good accordance with the NP distribution observed in Figs. 6 and 7.

Fig. 9 gives the illustration of the NP-induced refinement mechanism of primary Si. Firstly, a myriad of γ-Al_2O_3 NPs are dispersed in the melt via ultrasonic treatment, while some of the NPs inevitably agglomerate to form NP clusters in the melt. Then, as the melt temperature decreases, once the required degree of undercooling is reached, the nucleation of primary Si will proceed. For the solidification at low cooling rates, apart from some NP clusters acted as the heterogeneous nucleation sites for primary Si, the other individual NPs dispersed in the melt are pushed by the growing interface of primary Si to structure a uniform and dense NP-layer, thus inhibiting the solute transport to restrict the growth of primary Si. For the solidification at high cooling rates, the melt can provide a greater undercooling than the required critical one and thus a fraction of γ-Al_2O_3 NPs in the melt can work as effective nucleating particles for primary Si to promote its heterogeneous nucleation, resulting in a more striking refinement of primary Si. In the meanwhile, as a great majority of NPs may be engulfed by the growing interface of primary Si at high solidification rates, they are eventually distributed inside the matrix of primary Si. Overall, with increasing the solidification rate, the refinement mechanisms of primary Si changes from NP-induced growth restriction to NP-induced heterogeneous nucleation.

3.4. NP-induced modification mechanism of eutectic Si

Fig. 10 is the Schematic diagram of the modification mechanism for eutectic Si induced by NPs. Similar to the refinement of primary Si at low cooling rates, after the occurrence of the nucleation of eutectic Si

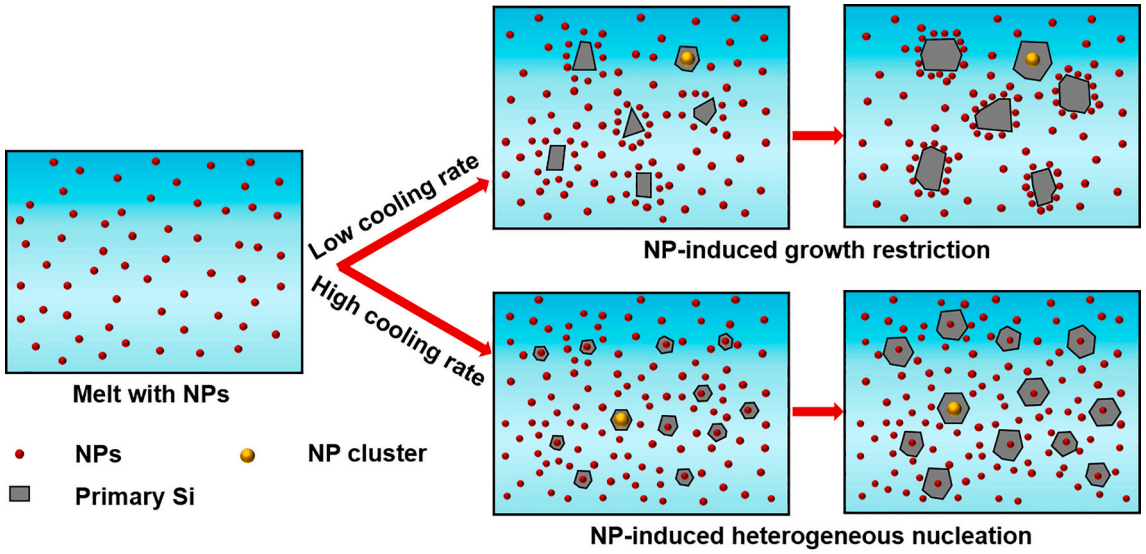

Fig. 9. Schematic diagram of the refinement mechanism for primary Si induced by NPs.

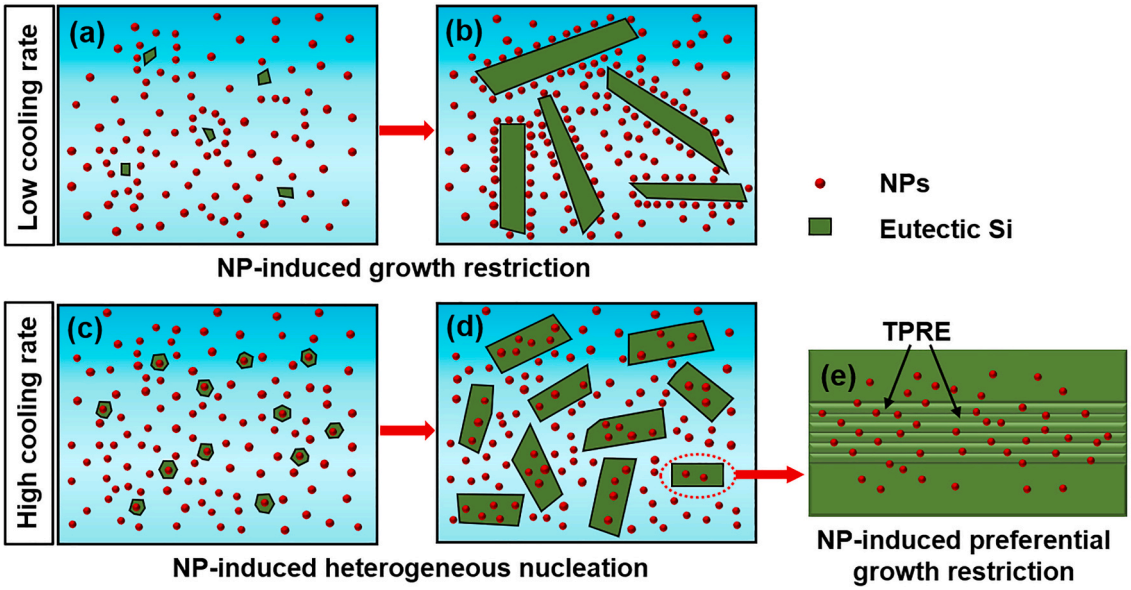

Fig. 10. Schematic diagram of the modification mechanism for eutectic Si induced by NPs.

(Fig. 10a), the NPs may also be pushed by the growth interface of eutectic Si due to low solidification rates, resulting in NP distribution along the eutectic Si phase boundary as displayed in Fig. 10b. A uniform and dense NP-layer covering the surface of eutectic Si can retard the solute transport and restrict its growth, thus triggering the refinement of eutectic Si particles. On the contrary, the growth velocity of eutectic Si may exceed the critical velocity during the rapid solidification. Thereby, many NPs would be captured by the growing interface of eutectic Si and distributed in the interior instead of the phase boundary (Fig. 10d). In addition to high cooling rate, viscous capture could also contribute to the NP captures in the eutectic Si zone where a number of γ-Al_2O_3 NPs are pushed [41]. It is inferred that the NPs embedded in the matrix of eutectic Si may have a crucial influence on the modification of eutectic Si particles. For one thing, given the good crystallographic matching

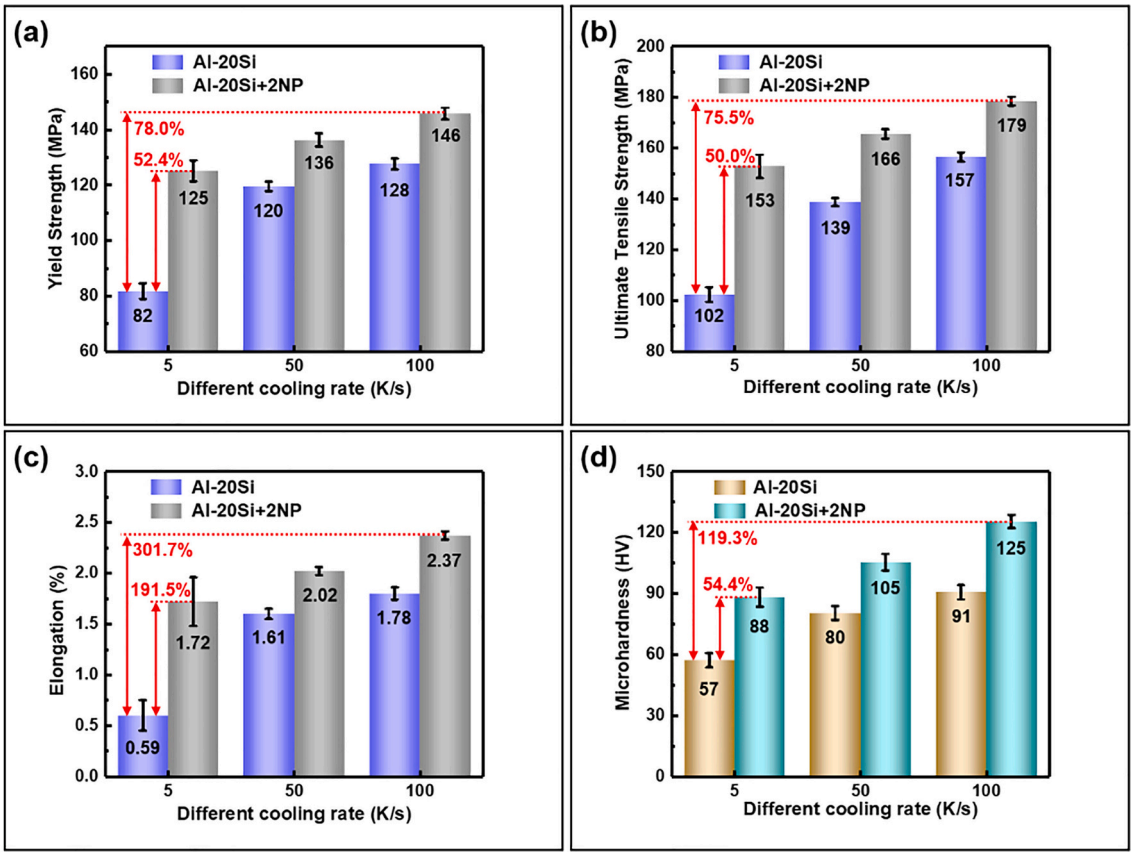

Fig. 11. Mechanical properties of Al-20Si alloys and Al-20Si + 2NP alloys with various cooling rates: (a) Yield Strength; (b) Ultimate Tensile Strength; (c) Elongation; (d) Microhardness.

relationship between γ-Al_2O_3 and eutectic Si as displayed in Fig. 7e, the γ-Al_2O_3 NPs may become the potent heterogeneous nucleating particles for eutectic Si. For another thing, the fast cooling processing can provide a larger melt undercooling for the heterogeneous nucleation of eutectic Si. Thereby, it is determined that NPs can serve as the effective nucleation sites for eutectic Si as illustrated in Fig. 10c, resulting in its refinement. Moreover, during the eutectic Si growth, a fraction of NPs that are captured at the TPRE in which the eutectic Si grows preferentially can stifle the preferential growth of eutectic Si as described in Fig. 10e. Because the growth variation of eutectic Si from the anisotropy to isotropy occurs, the growth advantage of TPRE is weakened greatly, inducing the eutectic Si modification. Conclusively, γ-Al_2O_3 NPs can refine the eutectic Si by restricting its growth at low cooling rates while they can modify it by promoting its heterogeneous nucleation and suppressing its preferential growth at high cooling rates.

3.5. Mechanical property evolution

Fig. 11a–c show the tensile properties of Al-20Si alloys and Al-20Si + 2NP alloys with various cooling rates. Thanks to the addition of 2.0 wt % NPs, the Al-20Si + 2NP alloys exhibit superior performance in strength and plasticity over the matrix alloy. Specifically, the yield strength and ultimate tensile strength of the Al-20Si + 2NP alloy at the cooling rate of 5 K/s reach 125 and 153 MPa, which are 52.4% and 50.0% higher than those of the matrix alloy. Elongation shows the same response to the NP addition as the yield strength and ultimate tensile strength. The 2.0 wt% NP additions can lead to the remarkable improvement in the ductility of the Al-20Si alloy, and the elongation of the Al-20Si + 2NP alloy at the cooling rate of 5 K/s is 1.72%, which is almost 2 times higher than that of the matrix alloy. Additionally, with increasing the cooling rate from 5 K/s to 100 K/s, it is clear that the yield strength, ultimate tensile strength and elongation of Al-20Si alloy are increased from 82 MPa, 102 MPa and 0.59% to 128 MPa, 157 MPa and 1.78%, respectively. Similar to the variation tendency for the Al-20Si + 2NP alloys, when the cooling rate rising up to 100 K/s, the yield strength, ultimate tensile strength and elongation of Al-20Si alloy are improved to 146 MPa, 179 MPa and 2.37%, respectively. The dependence of the microhardness of both alloys on the cooling rate is plotted in Fig. 11d. The microhardness increases nearly monotonically with the cooling rate. As the cooling rate ranges from 5 to 100 K/s, the microhardness of both alloys are increased from 57 and 88 HV to 91 and 125 HV, respectively. Compared with the NP-free Al-20Si alloy at the cooling rate of 5 K/s, the yield strength, ultimate tensile strength, elongation and microhardness of Al-20Si + 2NP alloy at the cooling rate of 100 K/s are increased by 78.0%, 75.5%, 301.7% and 119.3%, respectively.

Fig. 12 gives a series of TEM images regarding the Al-20Si + 2NP alloy produced at 50 K/s after a previous tensile deformation (0.2% strained). When the strain increases to 0.2%, the uneven deformation

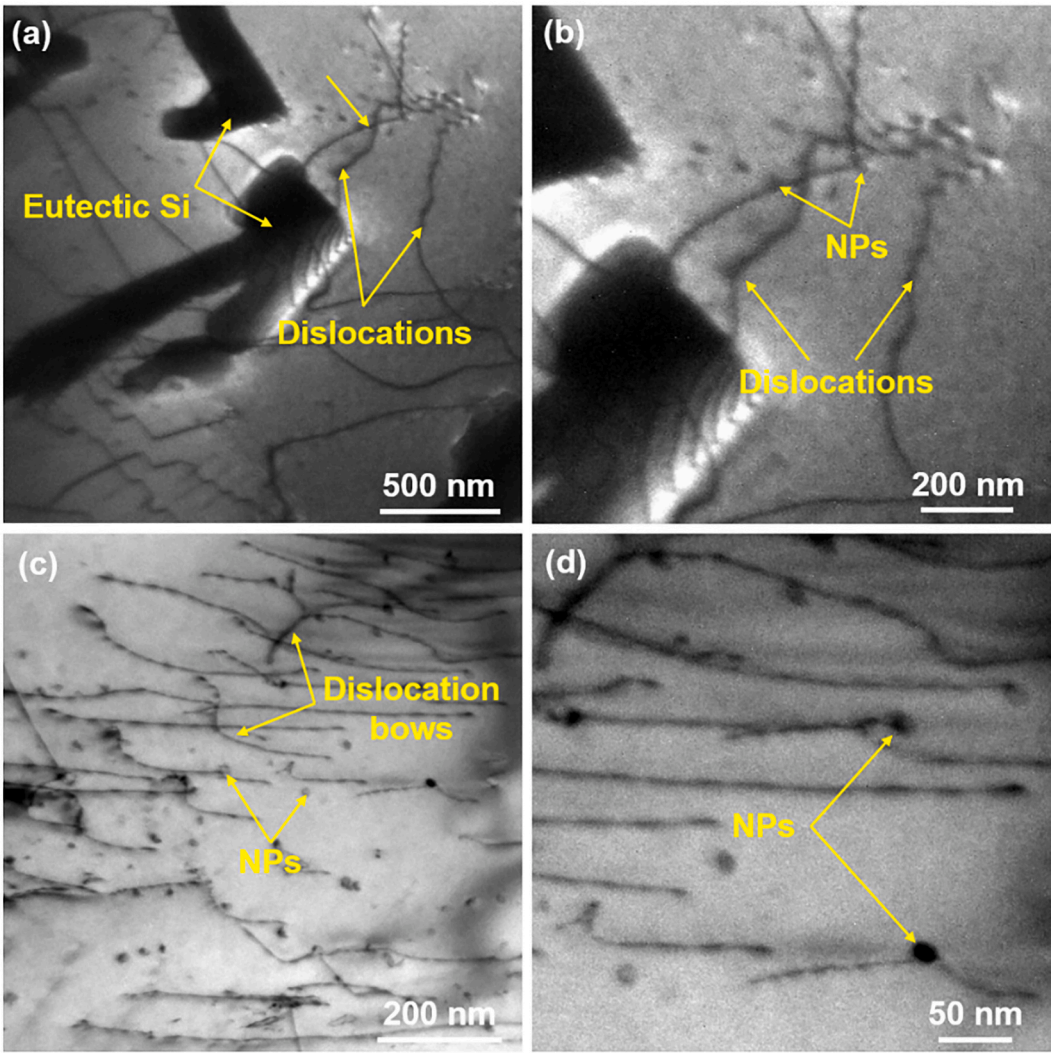

Fig. 12. TEM image of the Al-20Si + 2NP alloy solidified at the cooling rate of 50 K/s after 0.2% strained previous tensile deformation: (a) and (b) Dislocations near the Si particles; (c) and (d) Dislocations in the matrix.

between the particles and the matrix makes the stress concentrate near the refined eutectic Si particles during the scratching process, thus inducing the initiation of dislocations at the interface between the Si particle and the matrix, as displayed in Fig. 12a. In Fig. 12b, when the dislocations encounter NPs dispersed near the eutectic Si particle, these NPs pin the dislocations and hinder their motion during the subsequent plastic deformation. Meanwhile, it can be observed from Fig. 12c that there exists a large quantity of dislocations pinned by nanoparticles in the matrix. Further observation in Fig. 12d reveals that the dislocations are bypassing the NPs with the Orowan mechanism, thus leaving many dislocation bows. Studies [39,42] have demonstrated that dislocation bows are formed due to the resistance force imparted by NPs which relies on the bonding of NPs/matrix and the rigidity of NPs. Since γ-Al_2O_3 NPs are rigid, gliding dislocations cannot shear it. Combined with the well-coherent interface with the matrix, NPs dispersed in the matrix exhibit a strong resistance to dislocation motions, thus leading to a remarkable enhancement in the mechanical performance of Al-20Si alloys.

The enhanced mechanical properties might be dominantly attributable to the primary Si refinement and the eutectic Si modification along with the NP dispersion in the matrix. Moreover, further enhanced mechanical properties can be obtained via load transfer effect as well as Orowan strengthening due to dislocations pinning. Specifically, for grain refinement strengthening, the microstructure of the Al-20Si alloys is relatively complicated, including α-Al, primary Si and eutectic Si, which are all refined induced by NPs and high cooling rates. Thereby, it is difficult to evaluate the specific strength increment via Hall-Petch relationship. It can be determined that grain refinement does make a great contribution to the strength increment. For load transfer effect, according to the work of Nardon and Prewo [43], $\Delta\sigma_{load} = 0.5f\sigma_m$, where σ_m is the yield strength of the matrix alloy, and f is the volume fraction of γ-Al_2O_3 NPs. Therefore, the $\Delta\sigma_{load}$ has shown an increment of 0.55 MPa in yield strength. As for Orowan strengthening, the strengthening contribution caused by Orowan stress of γ-Al_2O_3 NPs can be expressed as $\Delta\sigma_{orowan} = \frac{0.13G_m b}{d_{NP}\left(\sqrt{3\frac{1}{2f}}-1\right)} ln\frac{d_{NP}}{2b}$ [44], where G_m is the shear modulus of the matrix alloy, b is the Burgers vector of the matrix, d_{NP} is the mean NP size. Considering that $G_m = 36$ GPa [45], $b = 0.202$ nm [45], $d_{NP} = 30$ nm. The contribution from Orowan strengthening is calculated to be 58.17 MPa. This result highlights the predominant role in strengthening the alloy of the Orowan strengthening.

4. Conclusion

In this work, the synergistic effects of NPs and cooling rates on the refinement and modification of Si particles in hypereutectic Al-20Si alloys were systemically investigated. The refinement and modification mechanisms of Si particles at different cooling rates have been analyzed and discussed, and the major findings are summarized as follows:

(1) The combination of γ-Al_2O_3 NPs and fast cooling processing can lead to the remarkable refinement of primary Si and modification of eutectic Si in hypereutectic Al-Si alloys. 2.0 wt% NP-containing Al-20Si alloy solidified at the cooling rate of 100 K/s exhibits the most refined and homogeneous microstructure. The average sizes of primary and eutectic Si minish significantly to 15.8 and 4.6 μm, respectively.

(2) The NP distribution changes with the solidification rate, i.e., an increment of solidification rate from 5 to 100 K/s may cause the transition of NP distribution from the Si phase boundary to the Si matrix mesoscopically and the transformation of the interface between the NP and the Si particle from incoherent to coherent microscopically.

(3) Refinement mechanism of primary Si and modification mechanism of eutectic Si also vary with the cooling rate: NP-induced growth restriction may be the main contributor for the refinement of primary and eutectic Si at low cooling rates; The NP-induced heterogeneous nucleation and preferential growth restriction of eutectic Si can account for the refinement and modification of primary and eutectic Si at high cooling rates, respectively.

(4) 2.0 wt% NP-containing Al-20Si alloy produced at 100 K/s exhibits the optimal mechanical properties with the yield strength, ultimate tensile strength, elongation and microhardness increased by 78.0%, 75.5%, 301.7% and 119.3%, respectively, as compared to the matrix alloy prepared at 5 K/s. The prominent enhancement in the mechanical performance of Al-20Si alloy may be dominantly attributable to the microstructural refinement and the reinforcing NPs dispersed in the matrix.

Data availability statement

All data included in this study are available upon request by contact with the corresponding author.

Declaration of Competing Interest

We declare that we do not have any commercial or associative interest that represents a conflict of interest in connection with the work submitted.

Acknowledgement

The present study was sponsored by the National Natural Science Foundation of China, People's Republic of China (NSFC) under Grant no. 51804197, Grant no. 51674166 and U1902220. Startup Fund for Youngman Research at SJTU (SFYR at SJTU).

Appendix A. Supplementary data

Supplementary data to this article can be found online at https://doi.org/10.1016/j.matchar.2021.111240.

References

[1] L. Lasa, J.M. Rodriguez-Ibabe, Effect of composition and processing route on the wear behaviour of Al-Si alloys, Scr. Mater. 46 (2002) 477–481.
[2] N. Tenekedjiev, J.E. Gruzleski, Hypereutectic aluminium-silicon casting alloys-a review, Cast Met. 3 (1990) 96–105.
[3] J. Sun, X.B. Zhang, Y.J. Zhang, N.H. Ma, H.W. Wang, Modification mechanism of primary silicon by TiB_2 particles in a TiB_2/ZL109 composite, J. Mater. Sci. 50 (2015) 1237–1247.
[4] Y.F. Xu, Y.Y. Chen, Z.P. Hu, J.Y. Wang, P. Schützendübe, Y. Huang, Y.C. Liu, Z. M. Wang, Microstructure evolution and interface structure of Al-40 wt% Si composites produced by high-energy ball milling, J. Mater. Sci. Technol. 35 (2019) 512–519.
[5] J.H. Jeon, J.H. Shin, D.H. Bae, Si phase modification on the elevated temperature mechanical properties of Al-Si hypereutectic alloys, Mater. Sci. Eng. A 748 (2019) 367–370.
[6] K. Wang, X. LV, Y.M. Zhu, H.Y. Jiang, Q.D. Wang, B. Ye, W.J. Ding, In-situ synthesis of novel Al-P-O master alloy and its refinement and modification effects on Si phases in hypereutectic Al-30Si alloys, Mater. Charact. 157 (2019) 109900.
[7] C.L. Xu, Q.C. Jiang, Y.F. Yang, H.Y. Wang, J.G. Wang, Effect of Nd on primary silicon and eutectic silicon in hypereutectic Al-Si alloy, J. Alloys Compd. 422 (1) (2006) L1–L4.
[8] J.H. Li, F.S. Hage, X.F. Liu, Q. Ramasse, P. Schumacher, Revealing heterogeneous nucleation of primary Si and eutectic Si by AlP in hypereutectic Al-Si alloys, Sci. Rep. 6 (2016) 1–8.
[9] K. Nogita, S.D. McDonald, K. Tsujimoto, K. Yasuda, A.K. Dahle, Aluminum phosphide as a eutectic grain nucleus in hypoeutectic Al-Si alloys, J. Electron Microsc. 53 (2004) 361–369.
[10] C.L. Xu, H.Y. Wang, F. Qiu, Y.F. Yang, Q.C. Jiang, Cooling rate and microstructure of rapidly solidified Al-20wt% Si alloy, Mater. Sci. Eng. A 417 (2006) 275–280.
[11] J.G. Jung, T.Y. Ahn, Y.H. Cho, S.H. Kim, J.M. Lee, Synergistic effect of ultrasonic melt treatment and fast cooling on the refinement of primary Si in a hypereutectic Al-Si alloy, Acta Mater. 144 (2018) 31–40.
[12] Z.Y. Cai, R.C. Wang, C. Zhang, C.Q. Peng, L.C. Xie, L.Q. Wang, Characterization of rapidly solidified Al-27Si hypereutectic alloy: effect of solidification condition, J. Mater. Eng. Perform. 24 (2015) 1226–1236.

[13] C.J. Todaro, M.A. Easton, D. Qiu, G. Wang, D.H. StJohn, M. Qian, Effect of ultrasonic melt treatment on intermetallic phase formation in a manganese-modified Al-17Si-2Fe alloy, J. Mater. Process. Technol. 271 (2019) 346–356.
[14] Q. Lan, C.L. Cheng, J.F. Zhang, R.Z. Guo, Q.C. Le, The relationship between the thermoelectric power and resultant solidification microstructures of Al-Si melt under electromagnetic field, Mater. Chem. Phys. 231 (2019) 203–215.
[15] Q. Zhang, X.F. Liu, H.S. Dai, Re-formation of AlP compound in Al-Si melt, J. Alloys Compd. 480 (2009) 376–381.
[16] Y.J. Xu, Y. Deng, D. Casari, R.H. Mathiesen, X.F. Liu, Y.J. Li, Revealing the nucleation kinetics of primary Si particles in hypereutectic Al-Si alloys under the influence of P inoculation, J. Mater. Sci. 55 (2020) 15621–15635.
[17] K. Wang, H.Y. Jiang, Q.D. Wang, Nanoparticle-induced nucleation of eutectic silicon in hypoeutectic Al-Si alloy, Mater. Charact. 117 (2016) 41–46.
[18] K. Wang, H.Y. Jiang, Q.D. Wang, W.J. Ding, Influence of nanoparticles on microstructural evolution and mechanical properties of Sr-modified Al-10Si alloys, Mater. Sci. Eng. A 666 (2016) 264–268.
[19] J. Eiken, M. Apel, S.M. Liang, R. Schmid-Fetzer, Impact of P and Sr on solidification sequence and morphology of hypoeutectic Al-Si alloys: combined thermodynamic computation and phase-field simulation, Acta Mater. 98 (2015) 152–163.
[20] Q.L. Li, T.D. Xia, Y.F. Lan, W.J. Zhao, L. Fan, P.F. Li, Effect of rare earth cerium addition on the microstructure and tensile properties of hypereutectic Al-20%Si alloy, J. Alloys Compd. 562 (2013) 25–32.
[21] Q. Li, T. Xia, Y. Lan, P. Li, L. Fan, Effects of rare earth Er addition on microstructure and mechanical properties of hypereutectic Al-20% Si alloy, Mater. Sci. Eng. A 588 (2013) 97–102.
[22] N. Raghukiran, R. Kumar, Effect of scandium addition on the microstructure, mechanical and wear properties of the spray formed hypereutectic aluminum-silicon alloys, Mater. Sci. Eng. A 641 (2015) 138–147.
[23] W.X. Shi, B. Gao, G.F. Tu, S.W. Li, Y. Hao, F.X. Yu, Effect of neodymium on primary silicon and mechanical properties of hypereutectic Al-15Si alloy, J. Rare Earths 28 (2010) 367–370.
[24] Q.L. Li, T.D. Xia, Y.F. Lan, W.J. Zhao, L. Fan, P.F. Li, Effect of in situ γ-Al_2O_3 particles on the microstructure of hypereutectic Al-20%Si alloy, J. Alloys Compd. 577 (2013) 232–236.
[25] H. Choi, H. Konishi, X. Li, Al_2O_3 nanoparticles induced simultaneous refinement and modification of primary and eutectic Si particles in hypereutectic Al-20Si alloy, Mater. Sci. Eng. A 541 (2012) 159–165.
[26] M. Acharya, A. Mandal, Individual and synergistic effect of gamma alumina (γ-Al_2O_3) and strontium on microstructure and mechanical properties of Al-20Si alloy, Trans. Nonferrous Metals Soc. China 27 (2019) 1353–1364.
[27] K. Wang, H.Y. Jiang, Y.X. Wang, Q.D. Wang, B. Ye, W.J. Ding, Microstructure and mechanical properties of hypoeutectic Al-Si composite reinforced with TiCN nanoparticles, Mater. Des. 95 (2016) 545–554.
[28] L. Zhang, S.Y. Chen, Q.C. Li, G.W. Chang, Formation mechanism and conditions of fine primary silicon being uniformly distributed on single α_{Al} matrix in Al-Si alloys, Mater. Des. 193 (2020) 108853.
[29] K. Wang, H.Y. Jiang, Y.W. Jia, H. Zhou, Q.D. Wang, B. Ye, W.J. Ding, Nanoparticle-inhibited growth of primary aluminum in Al-10Si alloys, Acta Mater. 103 (2016) 252–263.
[30] G.P. Xu, K. Wang, X.P. Dong, L. Yang, H.Y. Jiang, Q.D. Wang, W.J. Ding, Effects of titanium addition on the microstructural and mechanical property evolution of FeCrB alloys, Metall. Mater. Trans. A 51 (2020) 4610–4622.
[31] G.P. Xu, K. Wang, X.P. Dong, H.Y. Jiang, Q.D. Wang, B. Ye, W.J. Ding, Multiscale corrosion-resistance mechanisms of novel ferrous alloys in dynamic aluminum melts, Corros. Sci. 163 (2020) 108276.
[32] L.Y. Chen, J.Q. Xu, H. Choi, H. Konishi, S. Jin, X.C. Li, Rapid control of phase growth by nanoparticles, Nat. Commun. 5 (2014) 1–9.
[33] K. Wang, H.Y. Jiang, Q.D. Wang, B. Ye, W.J. Ding, A novel method to achieve grain refinement in aluminum, Metall. Mater. Trans. A 47 (2016) 4788–4794.
[34] T.F. Gu, Y. Pan, T. Lu, C.L. Li, J.H. Pi, Effects of boron addition on the morphology of silicon phases in Al-Si casting alloys, Mater. Charact. 141 (2018) 115–119.
[35] M. Qian, Heterogeneous nucleation on potent spherical substrates during solidification, Acta Mater. 55 (2007) 943–953.
[36] Z. Jian, X. Yang, F. Chang, W. Jie, Solid-liquid interface energy between silicon crystal and silicon-aluminum melt, Metall. Mater. Trans. A 41 (2010) 1826–1835.
[37] J.F. Hu, E.N. Pan, Determination of latent heat and changes in solid fraction during solidification of Al-Si alloys by the CA-CCA method, Int. J. Cast. Met. Res. 10 (1998) 307–319.
[38] D. Shangguan, S. Ahuja, D.M. Stefanescu, An analytical model for the interaction between an insoluble particle and an advancing solid/liquid interface, Metall. Trans. A. 23 (1992) 669.
[39] K. Wang, G.P. Xu, H.Y. Jiang, Q.D. Wang, B. Ye, W.J. Ding, Development of Al-TiCN nanocomposites via ultrasonic assisted casting route, Ultrason. Sonochem. 58 (2019) 104626.
[40] K. Wang, G.P. Xu, H.Y. Jiang, Q.D. Wang, W.J. Ding, Effects of $TiC_{0.5}N_{0.5}$ nanoparticles on the microstructure, mechanical and thermal properties of TiC0.5N0.5/Al-Cu nanocomposites, J. Mater. Res. Technol. 9 (2020) 2044–2053.
[41] J.Q. Xu, L.Y. Chen, H. Choi, X.C. Li, Theoretical study and pathways for nanoparticle capture during solidification of metal melt, J. Phys. Condens. Matter 24 (2012) 255304.
[42] K.M. Sree Manu, S. Arun Kumar, T.P.D. Rajan, M. Riyas Mohammed, B.C. Pai, Effect of alumina nanoparticle on strengthening of Al-Si alloy through dendrite refinement, interfacial bonding and dislocation bowing, J. Alloys Compd. 712 (2017) 394–405.
[43] V.C. Nardone, K.M. Prewo, On the strength of discontinuous silicon carbide reinforced aluminum composites, Scr. Metall. 20 (1986) 43–48.
[44] G.E. Dieter, Mechanical Metallurgy, third ed., McGraw-Hill, New York, 1986.
[45] P. Ma, Y.D. Jia, P.K. Gokuldoss, Z.H. Yu, S.L. Yang, J. Zhao, C.G. Li, Effect of Al_2O_3 nanoparticles as reinforcement on the tensile behavior of Al-12Si composites[J], Metals 7 (9) (2017) 359.